J Mater Sci (2009) 44:5815–5823
DOI 10.1007/s10853-009-3817-9

An investigation of mortars affected by alkali-silica reaction by X-ray synchrotron microtomography: a preliminary study

Nicoletta Marinoni · Marco Voltolini · Lucia Mancini · Pietro Vignola · Andrea Pagani · Alessandro Pavese

Received: 16 April 2009 / Accepted: 18 August 2009 / Published online: 2 September 2009

Abstract A first attempt to investigate samples affected by alkali-silica reaction (ASR) by synchrotron X-ray microtomography has been made. The setup available at the SYRMEP beamline, at the third generation synchrotron Elettra (Trieste, Italy), allowed collecting phase-contrast enhanced images, with a detectability approaching that of optical microscopy (a few microns). In this study, mortar cylinders were prepared and immersed in a 1-M NaOH solution at 80 °C for 14 days to enhance the ASR. The weathered samples were studied using the traditional 2D techniques such as optical microscopy and scanning electron microscopy as well as using the 3D micro-CT. Over the aged samples, the 3D imaging allows the ASR weathering to be studied, showing the reactive aggregate progressive dissolution with subsequent deposition of gel and microcracks development. This technique has proven to be a valuable, non-destructive, method which allows the rendering of the microstructural features in specimen affected by ASR.

N. Marinoni (✉) · A. Pagani · A. Pavese
Dipartimento di Scienze della Terra "Ardito Desio", Sezione di Mineralogia, Petrografia, Geochimica e Giacimenti Minerari, Università degli Studi di Milano, Via Botticelli 23, 20133 Milan, Italy
e-mail: nicoletta.marinoni@unimi.it

M. Voltolini · L. Mancini
SYRMEP Group, Sincrotrone Trieste S.C.p.A., S.S. 14, km 163,5 in Area Science Park, 34012 Basovizza, Trieste, Italy

P. Vignola · A. Pavese
Section of Milan, CNR—Istituto per la Dinamica dei Processi Ambientali, Via Mario Bianco 9, 20131 Milan, Italy

Introduction

Recently, synchrotron X-ray microtomography (micro-CT) has attracted much attention as a new method for the characterization of heterogeneous materials at the microscale [1]. This technique, by which a 3D volume of a sample is reconstructed from 2D projections taken at different angular steps, has proven to be very valuable for non-invasive investigation, at the micron scale, of small samples [2].

Over the last years, thanks to the technical advancements of micro-CT in synchrotron radiation facilities, many studies on cementitious materials have been performed [3–5]. Benz et al. [6, 7] report the first tomographic scans of cement pastes using synchrotron radiation, whereas recent researches by Helfen et al. [8] and Prometilla et al. [9] present a 3D reconstruction of cement paste during hydration in the former study and a quantification of tortuosity in hardened cement pastes in the latter one. A detailed review on the use of micro-CT on cement-based materials is reported by Burlion et al. [3]. The use of synchrotron X-rays, compared to the conventional laboratory sources, has many advantages [3] in particular the high spatial resolution (that can reach values lower than 1 μm) allows to obtain a detailed concrete microstructure characterization, thus playing a key role in defining the performance of cement-based materials [2].

To date, in spite the extensive works on concretes or mortars, surprisingly little is known on the use of synchrotron X-ray micro-CT on samples affected by alkali-silica reaction (ASR). The ASR is well-known weathering process of cement-based materials and consists of chemical reactions between silica aggregate, with different degrees of structural disorder (i.e. opal, chalcedony, chert, etc.), and the alkali and hydroxide ions in the pore water of concrete [10, 11]. The consequence of the ASR is the precipitation

of a gelatinous product, which promotes cracks and fractures through concretes, hardly affecting the material durability [12]. Different and complementary techniques are usually employed to investigate structures affected by ASR and the most commonly used are the optical and scanning electron microscopy [13, 14], limiting the information in the 2D.

This study is the first attempt on the use of micro-CT applied on cement-based materials weathered by ASR. The research aim is double-fold: on one side, we would like to demonstrate that X-ray synchrotron micro-CT is a viable, non-destructive technique for studying building materials affected by ASR; on the other side, we would investigate the mechanisms involved in the ASR, supplying thus a major step in the understanding of the ASR damage product formation.

This research has be carried out on mortar cylinders which were prepared by mixing an aggregate with Portland cement; the samples were then demoulded and immersed in a 1-M NaOH solution to speed-up the process of ASR gel formation. Additionally, the aggregate expansion potential towards ASR has been tested according to the standardized expansion test RILEM AAR-2 [15]. The aged samples were successively investigated by micro-CT and a comparison between the unweathered and weathered ones have been performed.

Materials

Specimens were prepared by mixing Ordinary Portland Cement (CEM I-42.5) with known contents of water and aggregate, the latter constituted by mudstone and chert fragments. The siliceous aggregate is angular in shape, with a size ranging from micro to crypto-crystalline with a few fossils whose hollows are preferentially filled by crypto-crystalline quartz and chalcedony. Carbonate fraction is wholly composed by micritic calcite. Mechanical sieving was used to separate the aggregates into two different fractions of 0.5 and 1 mm, respectively, so that they have a significant probability to be contained in the mortar cylinders.

Mortar samples approximately 50-mm high and 5 mm in diameter were prepared, with aggregates and cement paste ratio of 70:30% by volume and a water to binder ratio of 0.5 by weight. Two series of mortars have been prepared: the former consists of chert fragments only (hereafter labelled as mortar *A*) whereas the latter is obtained by mixing 50% chert and 50% mudstone (called mortar *B*). Cement and aggregates were mixed by hand for few minutes, then injected with a syringe into thin straws. The samples were then cured at 20 °C and 25% R.H. throughout the day, and subsequently at 50% R.H. during the following 27 days. After curing, the samples were removed from the straws and immersed into 1-M NaOH solution at 80 °C. Then, they were picked up after an ageing time of 1, 3, 7 and 14 days.

Experimental

Expansion testing

The aggregate reactivity has been tested according to RILEM AAR-2 [15]. Many of the experimental details have been provided in the Ref. [15], so that only a brief summary will be presented hereafter. As concerns the aggregate, it has been crushed down to sand-size (grain size that ranges from 125 μm and 4 mm), and graded according to the specified size outlined in RILEM protocol.

Three mortar prisms were prepared by mixing aggregate and cement OPC (CEM I-42.5) with a ratio of 2.25 and by considering a water–cement ratio of 0.47 by mass. Three mortar bars of $25 \times 25 \times 28.5$ mm^3 have been compacted. They were cured for 24 h in an environmental chamber at 95% RH and 20 ± 2 °C, then immersed in a closed container containing 1-M sodium hydroxide (NaOH) solution kept in a oven at 80 °C.

The average expansion of the mortar bars after 14 days of immersion in NaOH solution is used to estimate the reactivity of the aggregate. Generally, a 0.0–0.1% expansion means that the specific aggregate tested is not reactive, 0.1–0.2% is considered to be inconclusive and requires additional analysis. Three mortars bar test have been prepared to test the aggregate potential expansion according to RILEM AAR-2 [15].

Optical microscopy (OM)

The aged mortar bars were cut and thin sections were prepared according to Baumann [16] to evaluate what actually has expanded in the specimen. The samples have been investigated with an Ausjena Jenapol petrographic microscope [using transmitted illumination in plane polarised light (PPL) and cross-polarised light (XPL)] with magnifications ranging from 100 to 500× and the micrographs were acquired with a Nikon Coolpix 990 digital camera with an image resolution of 2600×2060.

Scanning electron microscopy (SEM)

Secondary electron (SE) images were performed using a Cambridge STEREOSCAN 360 scanning electron microscope (SEM) with an acceleration current of 15 kV, a beam size of ~100 nm and a working distance of 11 mm. The image resolution is of 1024×730 and 1.5 μm corresponds to 1 pixel.

Phase-contrast (PhC) imaging and X-ray computed microtomography (micro-CT)

Imaging with X-rays sample features close in size to the instrumental resolution and with similar mass absorption coefficients is a difficult task.

In conventional radiology, the image contrast is based exclusively on the detection of amplitude variation of the transmitted X-ray beam. The main restriction of this technique is the poor inherent contrast in samples with low-Z composition or with phases showing very small differences in mass density. PhC imaging, based on the observation of the *phase shifts* produced by the sample on the incoming wave, allows overcoming these limitations [17, 18]. For hard X-rays the phase component can be up to 1,000 times greater than the absorption one; therefore, it is possible to reveal phase effects even if the absorption is negligible.

Phase information can be accessed if the X-ray beam has a high spatial coherence as happens for third-generation synchrotron light sources [17–19]. In this case, the PhC radiography technique is based on free-space propagation and has a quite simple experimental application: contrary to the absorption mode where the sample is kept very close to the detector, in PhC mode the sample-to-detector distance D is usually in the range of 10–100 cm. The X-rays exiting from the sample propagate in the free space until they reach the detector. Free-space propagation transforms phase modulation of the transmitted beam into amplitude modulation. Contrast is originated from interference among parts of the wave-fronts that have experienced different phase shifts and it is related to Fresnel diffraction. According to the choice of D with respect to the size (a) of the feature to be identified perpendicularly to the beam direction, one may discriminate between two regimes: the edge detection regime ($D \ll a^2/\lambda$, where λ is the X-ray wavelength) and the holography regime ($D \approx a^2/\lambda$). The produced diffraction pattern appears superimposed to the conventional absorption pattern (if any) on the detector and contributes mainly to enhance the visibility of the edges of sample features modifying the local phase of the transmitted X-ray beam (phase objects), such as inclusions, pores, interfaces between regions with different mass density. In the edge detection regime, the images can be used directly to extract morphological information from the analysed sample. In the holography regime, it is possible to access phase information but a deformed image of the sample features is obtained.

The hard X-ray imaging experiments were performed at the SYRMEP beamline of the third-generation synchrotron light source (Elettra) located in Trieste (Italy). The X-ray source is one of the bending magnets of Elettra and the beamline provides, at a distance of about 23 m from the source, a monochromatic, laminar-section X-ray beam with a maximum area of about 160×6 mm^2. The monochromator is based on a double Si(111) crystal system working in Bragg configuration that can be tuned in an energy range of 8.3–35 keV with an energy resolving power of about 10^{-3}.

Due to the small source size, the distance between the source itself and the sample position, and the simple design of the beamline, the photon spot in the experimental hutch is characterized by a good level of spatial coherence (transversal coherence length of about 10 μm at 15 keV) then allowing to perform PhC imaging by using free-space propagation.

For micro-CT investigations samples were mounted on a high-resolution rotation stage and illuminated with a monochromatic radiation ($E = 25$ keV). For each tomographic scan, 1,440 projections of the sample were acquired for equally spaced rotation angles and measurement time of about 1 s over a total rotation of 180°. The projections were recorded using a 12/16-bit water cooled CCD camera, 4008×2672 pixels^2, 9×9 μm^2 pixel size, coupled to (1:2) tapered magnifying optics. In this case, an active input area of 18 (h) × 12 (v) mm^2 is imaged on the sensor. In order to reconstruct a 3D image of the sample, the tomographic projections were elaborated using a custom-developed software written in IDL® language and based on a filtered backprojection algorithm [20]. The 2D reconstructed slices were visualized using the ImageJ freeware software [21].

When applying hard X-rays imaging techniques to material science, care is needed to choose the proper sample-to-detector distance D (usually related to the nature of sample) to have a suitable signal: a sample too close to the detector will have interference fringes barely visible, on the other hand if the distance is too large, many interference fringes will be visible at the edges. Then, small phase objects would appear deformed and the finest details would be not visible. Therefore, setting the correct working distance is of paramount importance for visualizing these small objects, such as the gel-filled microcracks in our samples, and different distances need to be checked to choose the better one. An example is shown in Fig. 1, where two different D values have been set to analyse the mortar cylinder A aged for 14 days. Two different datasets have been collected keeping all the parameters fixed except for the distance D: 5 cm in Fig. 1a and 20 cm in Fig. 1b. Two slices reconstructed at exactly the same height of the sample are shown to highlight the differences. Looking at the whole slices it is possible to observe how the image in Fig. 1b looks less "blurry" and how the smaller details are better resolved. In particular, it is possible to detect more details, e.g. the dried gel phase in the voids left by the corroded chert; the smaller cement paste pores and the grains interfaces are sharper. On the other hand, looking at the two close-ups of the slices a dramatic difference is

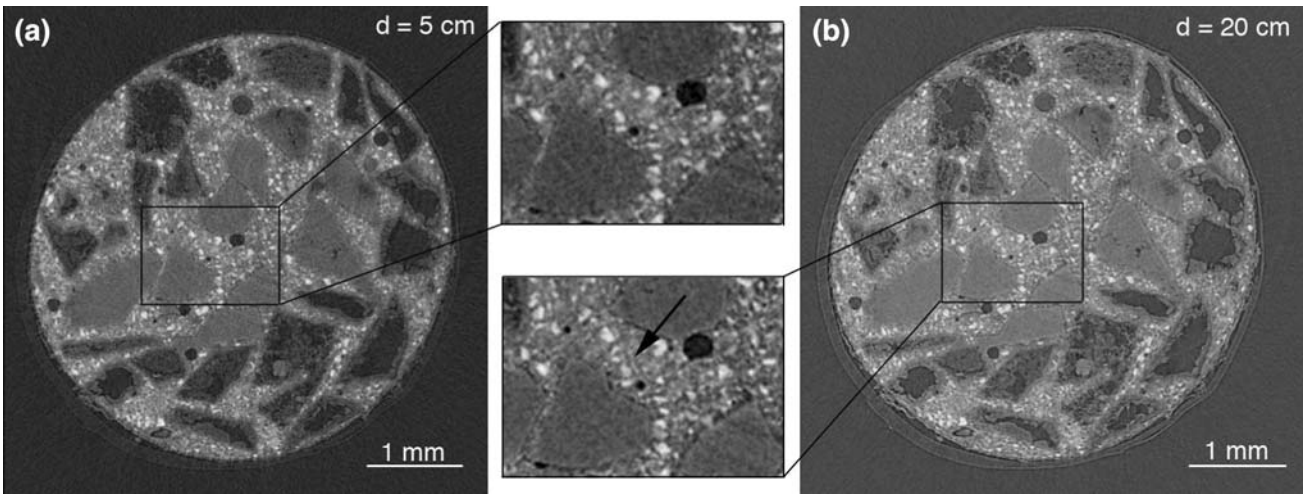

Fig. 1 2D visualisation of mortar *A* aged for 14 days: the two slices were collected with a the sample-detector distance of 5 cm in (**a**) and 20 cm in (**b**)

noted: in the slice reconstructed from the dataset collected at 20 cm a microcrack connecting two aggregate grains and passing through a little bubble is visible (indicated by the arrow), while in the other slice no evidence of this microcrack is present. Hence the importance of choosing the correct *D* value while analyzing such potentially troublesome samples [19].

Digital image processing (DIP)

Image analysis has proven to be a reliable technique to investigate microcracks in cement-based materials [22, 23]. In the study herein presented, the orientation of microcracks has been performed by an automated image analysis applied to SEM images where microcrack networks due to ASR are clearly visible (see in the next section Fig. 2a). To obtain a meaningful statistics eight images were selected for the image analysis [22]. A proper threshold value was selected for segmentation of the microcracks (see segmented image in Fig. 2b) by a segmentation algorithm based on statistical inference. After segmentation triple points of the microcrack network were erased to obtain isolated single cracks. A conventional second-order momentum analysis was then applied to the objects and the orientation of the cracks is plotted in polar graph showing an orientation rosette. Cracks show little preferred orientation. The whole image analysis has been done using a custom-made MATLAB® script.

Results and discussion

The expansion tests revealed that, after 14 days, chert aggregates largely exceeded the limit for potentially deleterious expansion. The optical analyses on the mortar bars pointed out the presence of micrometric microcracks, which develop both into the aggregate grains and cement paste. The magnitude of the crack opening was larger in cement paste than in the aggregate. Cracks at the cement-paste–aggregate boundaries did not have chance to evolve whereas they formed extensively in the matrix area. In the 14-day aged samples chert fragments with irregular and poorly distinct edges have been observed, suggesting that ASR has taken place at the cement–aggregate boundaries involving, thus the dissolution of the siliceous aggregate (Fig. 3a, b). These observations are also corroborated by SEM analysis: thanks to the large magnification employed by the electron microscope, the widespread microfracture systems are clearly detected (Fig. 2a) and the application of the digital image processing allows to define the microcracks orientation within the cement paste. In particular, in Fig. 2b the cement paste appears to be interested by a large number of micrometric fractures showing a close to random orientation (Fig. 2c), commonly known as map-cracking [12]. These results attest that OM and SEM analyses can be considered powerful methods for investigating cement-based materials affected by ASR. On the other hand, their main shortcomings are the lack of 3D information (for instance the cracks real size and spatial distribution are lost) and sample preparation, the latter being very laborious and potentially invasive. In contrast, X-ray micro-CT is a technique by which a 3D reconstruction is available without requiring a large amount of time for specimen preparation.

In this study, mortars *A* and *B* aged up to 14 days have been investigated by X-ray synchrotron micro-CT. In Fig. 4a comparison between an unreacted and reacted mortar is shown. In particular, Fig. 4a reports an example

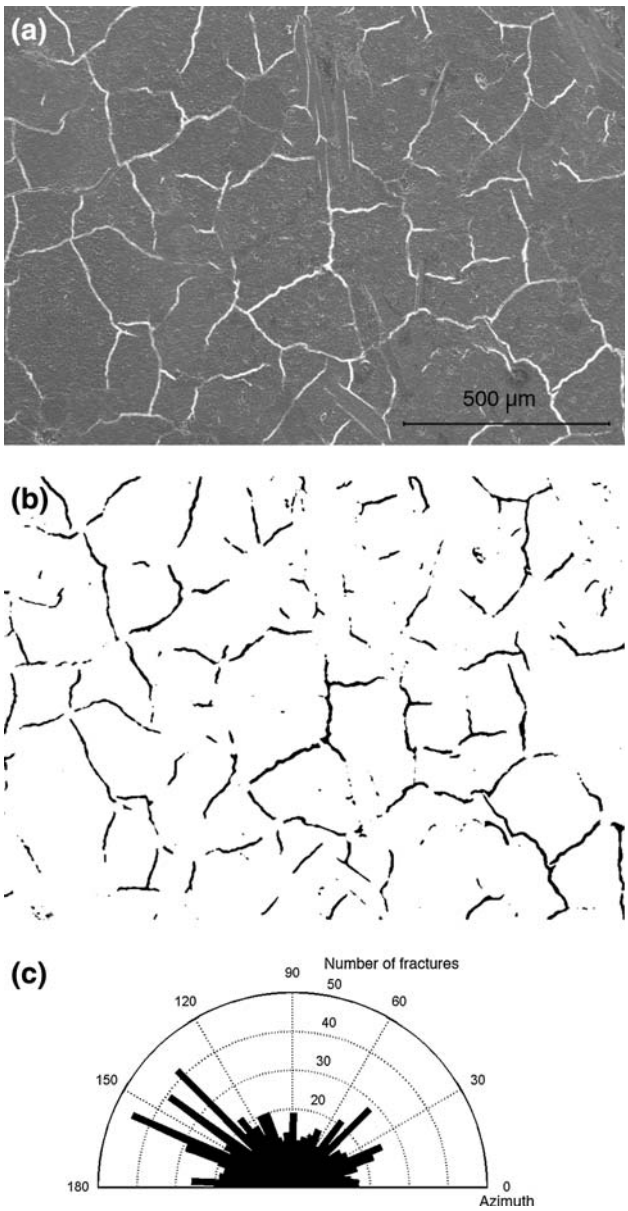

Fig. 2 **a** Backscattering SEM image of the microcracks network in the cement paste due to ASR; **b** the image above after a threshold filter to highlight the microcracks; **c** polar diagram showing the orientation rosette of the microcracks (eight images were used to obtain this orientation distribution). This image analysis refers to the 14-day aged mortar *A*

of no aged mortar from which it is evident that the aggregate fraction as well as cement paste and porosity exhibit different grey level histograms so that they can be easily differentiated. No microcracks are detected whereas only voids and bubbles due to mortar preparation can be identified. Conversely, Fig. 4b was taken just after 14 days of aging and showed additional voids, angular in shape and with an irregular surface, which are more likely related to the gel formation and subsequent drying due to the corrosion of chert fragments. Unfortunately, it has proven difficult to extract morphological information on microcracks because of their small size. Hence, the ASR gel filling them with a material with higher mass absorption coefficient than air creates additional problems in visualizing the cracks with size close to the instrumental resolution [see (b) inset with a close-up of a microcrack and for details see "Phase-contrast (PhC) imaging and X-ray computed microtomography (micro-CT)"]. Gallucci et al. [2] first report the same difficulty in visualizing smaller pores and microcracks during OPC paste aging because of C–S–H gel filling.

In Fig. 5, the 3D visualization of mortar *A* aged for 7 days has been reported and only one half of the sample is shown for easily detecting its features at microscale. In particular in Fig. 5a, the isosurface of the voids is plotted in blue colour whereas a greyscale isocap has been added to better visualize the chert aggregate in Fig. 5b. Small voids surrounding the aggregate grains owing to the ASR at the chert surface are shown; indeed, small cavities occur inside the grains, presumably because of discontinuities with higher reactivity and/or easier fluids migration properties (planar defects, cracks, etc.). Figure 5c and d represents a close-up of the volume with a chert grain and the volume position within the sample is highlighted with the box in (a) and (b), respectively (note that the latter has been rotated by 90° to enhance the visualization); a transparent greyscale isocap is added to better visualize the relationship of the voids with respect to the aggregate particle; it is clear that that the smaller voids, due to the chert weathering, surrounded the whole surface of the aggregate particle; moreover, their shape appears quite different (more irregular) from the spherical and bigger bubbles related to the mortar porosity. As concerns mortar *B* aged for 7 days, the chert weathering is consistent with the one observed in mortar *A*; therefore, for sake of brevity, no figures will be therein reported.

At 14 days of aging, the dissolution of chert fragment is found to occur within the mortar samples. In Fig. 6a and b, chert surface seems to be characterized by irregular hole due to dissolution owing to ASR. In Fig. 6c and d, two meaningful subvolumes are plotted (the latter slightly rotated for a better visualization) and it is clearly seen that the chert grains appear partially dissolved with deeply corroded boundaries and where only their inner part seems to be preserved.

By comparing Figs. 5 and 6, we can assess that, as the aging time increases, the volume formerly occupied by the chert particles becomes almost empty. The dried ASR gel deposition into voids is also observed, encouraging their surface to become very rough and irregular; indeed, the pore surface within mortars, originally well rounded in shape, becomes slightly rougher because of the presence of dried gel filling them.

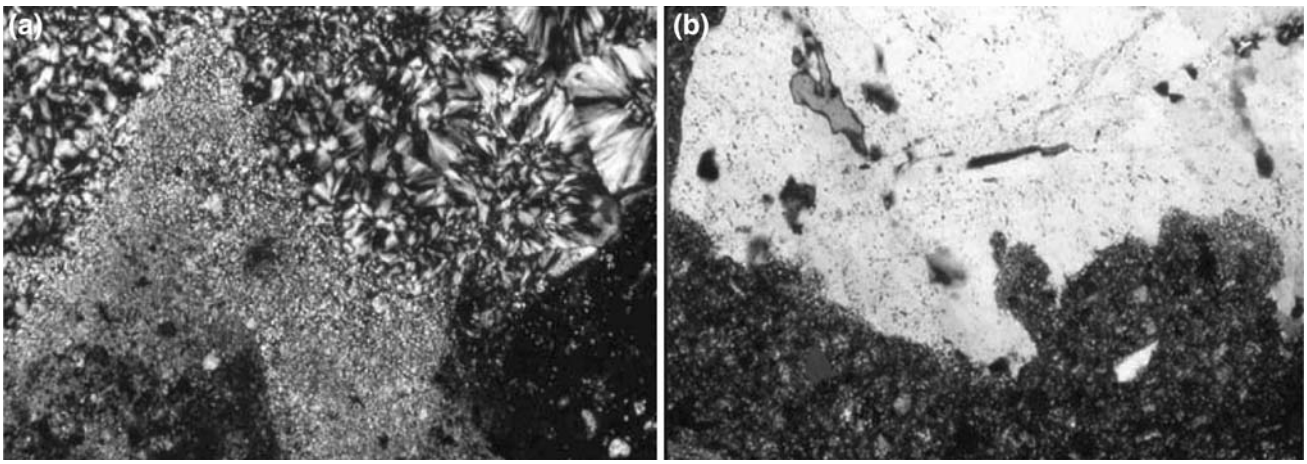

Fig. 3 Optical micrographs: **a** chert fragments with irregular boundaries (XPL, ×25); **b** chert fragment highly corroded in shape (PPL, ×25) (mortar *A* aged for 14 days)

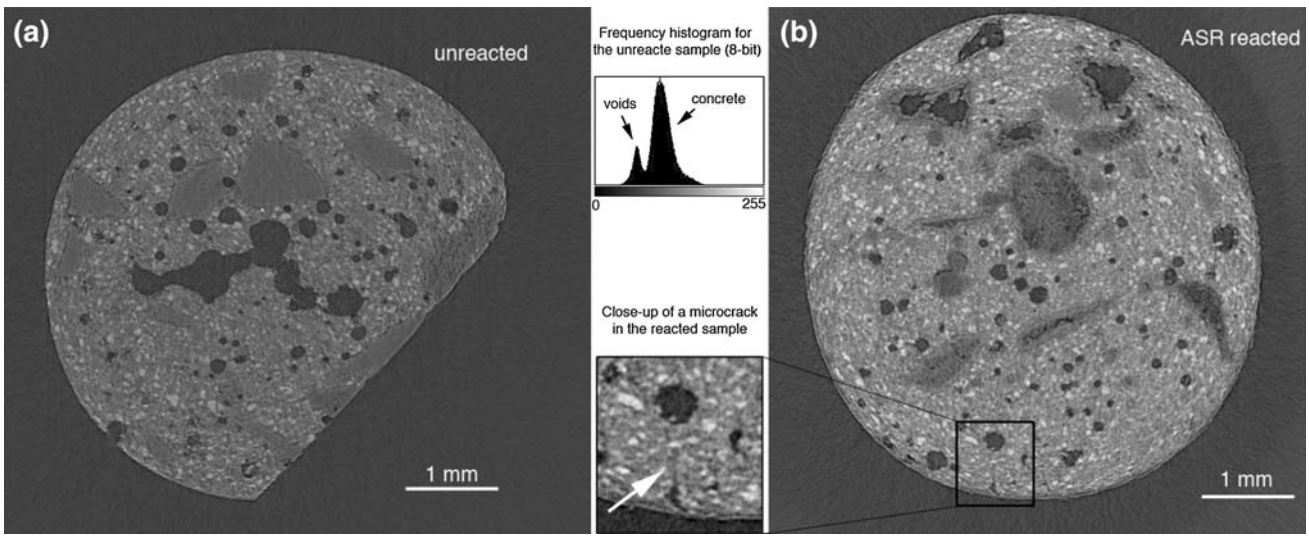

Fig. 4 Reconstructed slices from the micro-CT experiment. In **a** an unreacted mortar and in **b** a reacted one (aged for 14 days) are reported

In Fig. 7a, the rendering of voids-solids isosurface in mortar *B* aged for 14 days is shown. In agreement with the previous figure, the porosity of mortars and voids due to the chert dissolution are clearly differentiated. Since the grey levels of limestone (lighter grey levels) and chert (now voids indicated by the blue isosurface) (Fig. 7b) are markedly different because of different mass absorption coefficient of calcium carbonate with respect to the other mortar components; an additional threshold level could be added to isolate limestone aggregate from the whole (Fig. 7c). Note that cement phases have grey levels close to the ones of limestone, but easily recognized because of their smaller size. In the present figures limestone grains appear to be not reactive, exhibiting large subvolumes without any voids; this implies that that no grain surface pores as well as limestone aggregate surface detachment from the cement paste are observed. In (d) a close-up of a bigger chert particle is plotted, appearing partially dissolved with an angular shape and an extremely rough surface due to ASR attack. Finally in Fig. 7e, a small subvolume with two isosurfaces highlighting voids (blue) and highly absorbent phases (limestone aggregate and some cement phases, plotted in yellow) is shown: in particular a small chert particle wholly weathered (on the left) is associated to a bigger limestone particle (without any void on the surface) and the small highly absorbent cement phase grains regularly distributed into the cement paste. Therefore, we may assume that as the aging time increases, the chert dissolution leads to a strong increase of the sample porosity, which amplifies the accessibility of external dissolution to sound material, thus enhancing the degradation phenomena.

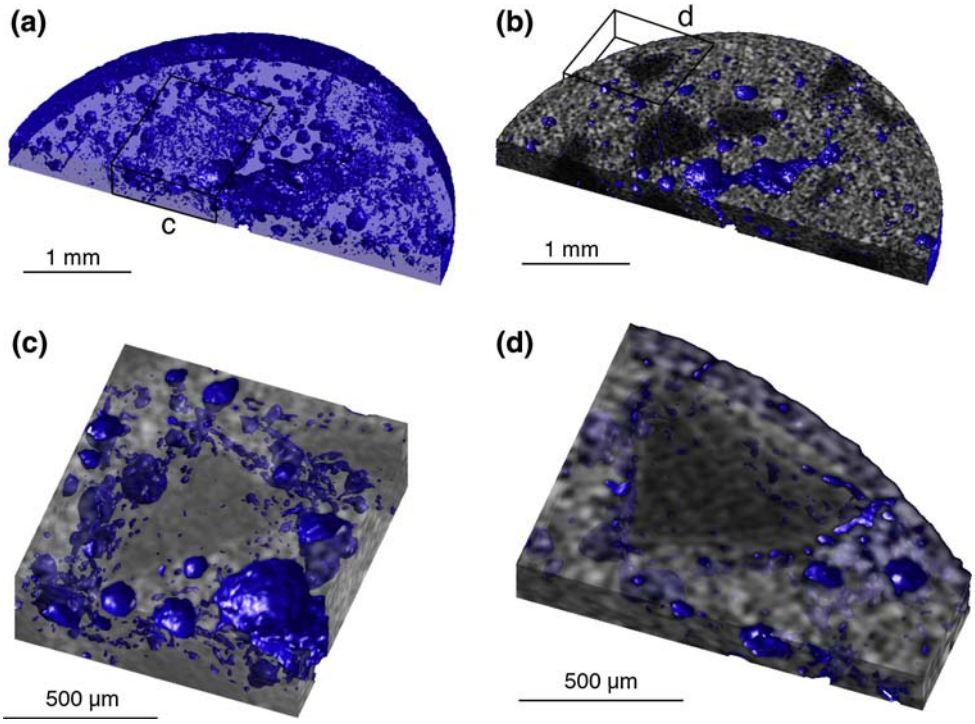

Fig. 5 3D visualization of mortar *A* weathered for 7 days. In **a**, **b** half size of sample is shown whereas **c**, **d** are zoomed part of box (*c*) and (*d*) in (**a**) and (**b**), respectively

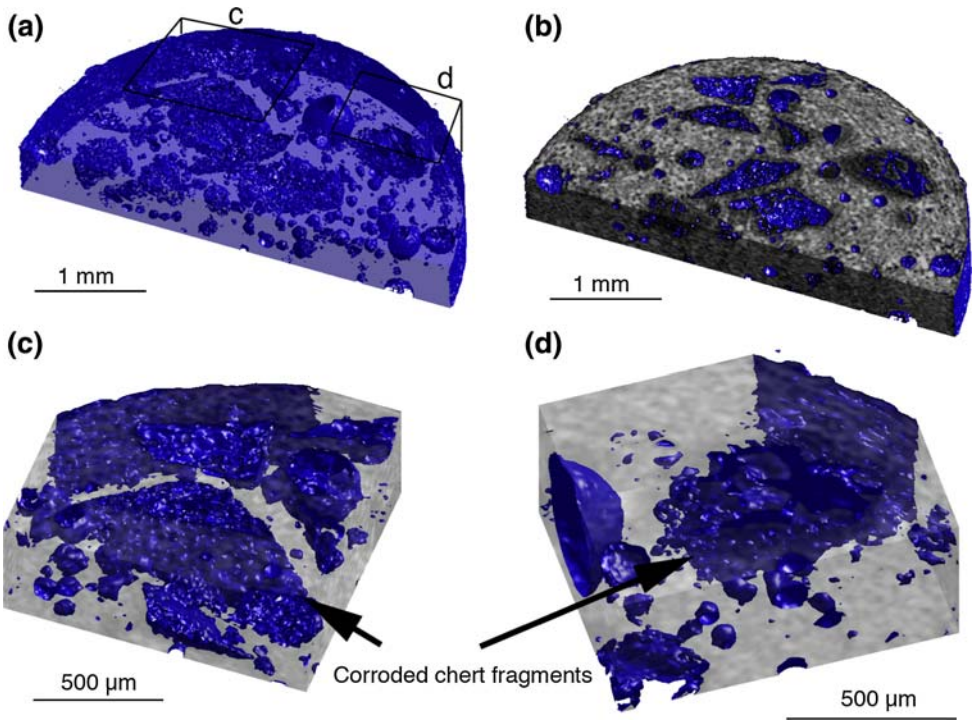

Fig. 6 3D visualization of mortar *A* weathered for 14 days. In **a**, **b** half size of sample is shown whereas **c**, **d** are zoomed part of box (*c*) and (*d*) in (**a**)

Moreover, the reconstructed volumes have allowed obtaining the 3D visualization of microcracks; although, it has proven difficult to observe them as reported in "Phase-contrast (PhC) imaging and X-ray computed microtomography (micro-CT)". First of all, we want to emphasize the ability of the phase-contrast setup to detect small features in samples where the conventional absorption setup is not enough to resolve features so small or interfaces between materials with similar mass absorption coefficients, as shown in our materials. The slices presented in Fig. 1 clearly show how the proper experimental setup can make a huge difference. In this case, the microcracks are close in size to the detector resolution (pixel size = 9 µm); the effect of the phase contrast permits to enhance the detail

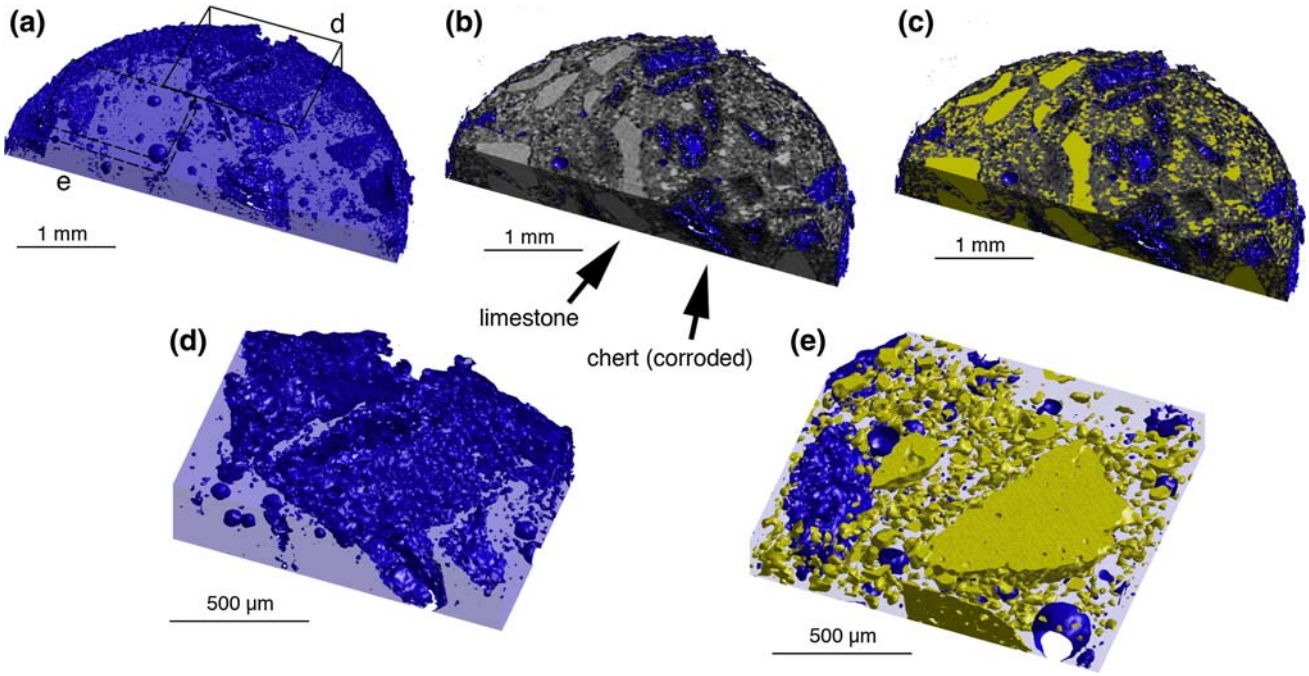

Fig. 7 3D visualization of mortar *B* weathered for 14 days In **a**–**c** half size of sample is shown whereas **d**, **e** are zoomed part of box (*d*) and (*e*) in (**a**)

detectability close or even below the constraints given by the detector resolution.

In this study, the 3D shape of microcracks can be obtained from the extracted slices of the complete tomographic dataset via a segmentation process. In the unweathered samples no cracks are detected, whereas they appear in the specimen aged for 14 days only (Fig. 8a) and are associated with chert fragment dissolution (Fig. 8b). In Fig. 8c and d, two subvolumes showing details of the superficial microcrack plotted in Fig. 8a are shown: it is clearly seen that the main part of the cracks in the cement paste looks almost flat and inclined, whereas the ones close to the dissolved aggregate seem much more tortuous, showing more complex pattern (zoomed box c). Further

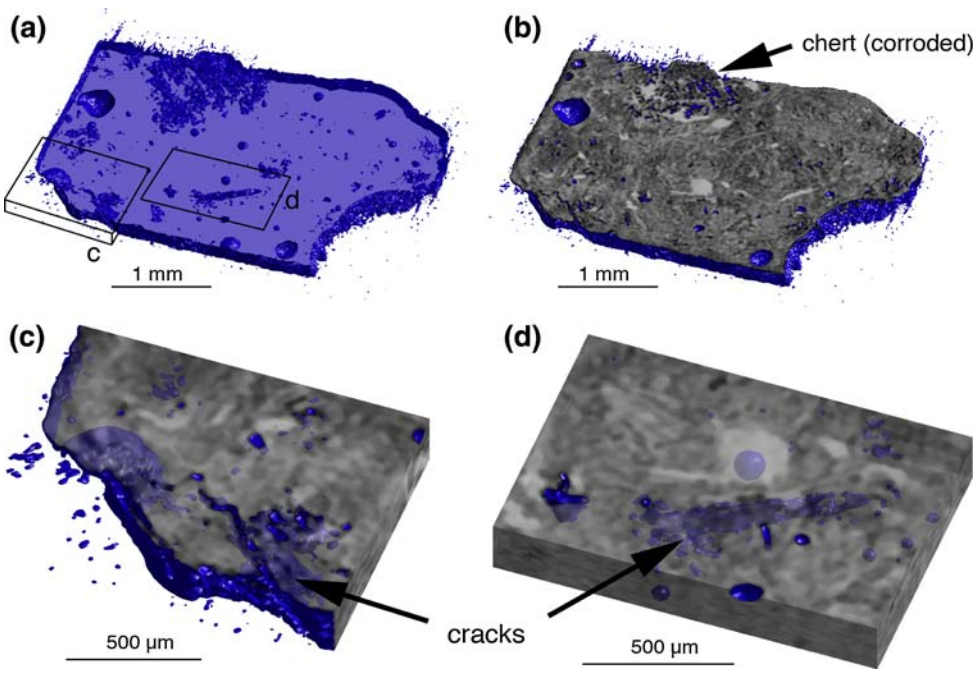

Fig. 8 3D visualization of mortar *A* weathered for 14 days: **a**, **b** refer to a portion of mortar sample whereas **c**, **d** are zoomed part of box (*c*) and (*d*) in (**a**)

enhancements of the obtainable data will be possible with a detector with a smaller pixel size for obtaining 3D mapping of microcracks due to ASR.

On the basis of the above qualitative observations, we can assess that, as the aging time increases, the ASR induces first the dissolution of chert fragments, thus enhancing the mortar porosity and later the growth of microcracks. On the other hand, no weathering phenomena are observed on limestone aggregate, which is inert to ASR.

Conclusion

In this research, we report a preliminary study on the use of synchrotron X-ray micro-CT on cement-based materials affected by ASR. In particular, thanks to the new third-generation synchrotron X-ray sources at the beamline SYRMEP at Elettra (Trieste, Italy) a spatial resolution of a few microns has been achieved, thus allowing to investigate the microstructural features of mortars affected by ASR.

Mortar samples, aged from 1 to 14 days in a 1-M NaOH solution, have been investigated; the 3D reconstructions highlight the chert dissolution during the weathering as well as the occurrence of microcracks in the cement paste. Indeed, the visualization of 3D volumes has allowed gathering qualitative information, such as cracks real size, spatial distribution, in contrast to the traditional 2D analytical methods where these microstructural features are inaccessible.

Therefore, synchrotron X-ray micro-CT has demonstrated itself to be a valuable tool for the observation of the microstructural features within hardening cement-based materials affected by ASR. Further studies are in progress to extract quantitative data, such as crack pattern within the cement paste, crack connectivity and topology within weathered mortar owing to ASR by X-ray micro-CT investigations.

Acknowledgement The authors would also like to thank N. Sodini for his precious technical help at the SYRMEP beamline at the Elettra synchrotron facility during data collection.

References

1. Ashbridge DA, Thorne MS, Rivers ML, Muccino JC, O'Day PA (2003) Comp Geosci 29:823
2. Gallucci E, Scrivener K, Groso A, Stampanoni M, Margaritondo G (2007) Cem Concr Res 37:360
3. Burlion N, Bernard D, Chen D (2006) Cem Concr Res 36:346
4. Lu S, Landis EN, Keane DT (2006) Mater Struct 39:611
5. Naik NN, Jupe AC, Stock SR, Wilkinson AP, Lee PL, Kurtis KE (2006) Cem Concr Res 36:144
6. Bentz DP, Mizell S, Satterfield S, Devaney J, George W, Ketcham P, Graham J, Porterfield J, Quenard D, Vallee F, Sallee H, Boller E, Baruchel J (2002) J Res Natl Inst Stand Technol 107:137
7. Bentz DP, Quenard DA, Kunzel HM, Baruchel J, Peyrin F, Martys NS, Garboczi EJ (2000) Mater Struct 33:147
8. Helfen L, Dehn F, Mikulik P, Baumbach T (2003) Synchrotron radiation X-ray tomography: a method for the 3D verification of cement microstructure and its evolution during hydration. In: Proceeding of the first international congress on nanotechnologies in the construction industry, Glasgow
9. Promentilla MAB, Sugiyama T, Hitomi T, Takeda N (2009) Cem Concr Res 39:548
10. Swamy N (1992) The alkali-silica reaction in concrete. Blackie, London
11. Pire DC (1990) Standards for aggregates. Ellis Horwood, London
12. Hobbs DW (2002) In: Bensted J, Barnes P (eds) Structure and performance of cements. E & FN Spon, London
13. Thaulow N, Hjorth JU, Boyd C (1996) Cem Concr Res 26:309
14. Delem L, Van Dam T, Peterson KL, Sutter L (2004) J Trans Res Board 1893:11
15. RILEM (2000) Mater Struct 33:283
16. Baumann HN (1957) Am Mineral 2:416
17. Snigirev A, Snigireva I, Kohn V, Kuznetsov S, Schelokov I (1995) Rev Sci Instrum 66:5486
18. Cloetens P, Barrett R, Baruchel J, Guigay JP, Schlenker M (1996) J Appl Phys 29:133
19. Mancini L, Reinier E, Cloetens P, Gastaldi J, Härtwig J, Schlenker M, Baruchel J (1988) Phil Mag A78:1175
20. Herman GT (1980) Image reconstruction from projections. Elsevier, New York
21. Abramoff MD, Magelhaes PJ, Ram SJ (2004) Biophotonics Int 11:36
22. Marinoni N, Pavese A, Foi M, Trombino L (2005) Cem Concr Res 35:1613
23. Ammouche A, Breysse D, Hornain H, Didry O, Marchand J (2000) Cem Concr Res 30:25